



LAWRENCE
LIVERMORE
NATIONAL
LABORATORY

Mitigation of upward and downward VDE heat loads with upper or lower massive gas injection in DIII-D

E. M. Hollmann, N. Commaux, N. W. Eidetis, C. J. Lasnier, R. A. Moyer, P. B. Parks, D. Shiraki

April 16, 2015

Physics of Plasmas

Disclaimer

This document was prepared as an account of work sponsored by an agency of the United States government. Neither the United States government nor Lawrence Livermore National Security, LLC, nor any of their employees makes any warranty, expressed or implied, or assumes any legal liability or responsibility for the accuracy, completeness, or usefulness of any information, apparatus, product, or process disclosed, or represents that its use would not infringe privately owned rights. Reference herein to any specific commercial product, process, or service by trade name, trademark, manufacturer, or otherwise does not necessarily constitute or imply its endorsement, recommendation, or favoring by the United States government or Lawrence Livermore National Security, LLC. The views and opinions of authors expressed herein do not necessarily state or reflect those of the United States government or Lawrence Livermore National Security, LLC, and shall not be used for advertising or product endorsement purposes.

Mitigation of upward and downward VDE heat loads with upper or lower massive gas injection in DIII-D

E.M. Hollmann¹, N. Commaux², N.W. Eidietis³, C.J. Lasnier⁴, R.A. Moyer¹, P.B. Parks³, and D. Shiraki²

¹ University of California-San Diego, La Jolla, California, 92093, USA

² Oak Ridge National Laboratory, Oak Ridge, Tennessee, 37831, USA

³ General Atomics, San Diego, California, 92186, USA

⁴ Lawrence Livermore National Laboratory, Livermore, California, 94550, USA

Abstract

Intentionally triggered upward and downward vertical displacement events (VDEs) leading to disruptions were pre-emptively mitigated with neon massive gas injection (MGI) coming from either above or below the plasma. Global indicators of disruption mitigation effectiveness (conducted heat loads, radiated power, and vessel motion) do not show a clear improvement when mitigating with the gas jet located closer to the VDE impact area. A clear trend of improved mitigation is observed for earlier MGI timing relative to the VDE impact time. The plasma current channel is seen to lock to a preferential phase during the VDE thermal quench, but this phase is not clearly matched by preliminary attempts to fit to the conducted heat load phase. Clear indications of plasma infra-red emission are observed both before and during the disruptions; this infra-red emission can affect calculation of disruption heat loads.

1. Introduction

Disruptions can occur in tokamaks if a plasma discharge is moved past stability boundaries or due to a failure in the plasma control system. In the case of control system failure, vertical displacement event (VDE) disruptions are a typical outcome, due to the vertical instability of elongated tokamak plasmas. Conducted loads resulting from unmitigated disruptions are predicted to cause unacceptable levels of damage to first wall components in future large tokamaks due to heat fluxes up to GW/m^2 [Hender2007, Hollmann2011], thus requiring mitigation by pre-emptive impurity injection to increase the radiated power fraction. To-date the most studied impurity injection methods are massive gas injection (MGI) [Taylor1999] and shattered pellet injection (SPI) [Commaux2010]. Requirements for mitigation of disruption conducted heat loads in ITER are quite stringent, with a goal of $> 95\%$ radiated energy fraction in mitigated ITER disruptions. With this high radiated energy fraction, beryllium wall melting could occur in ITER if the toroidal peaking factor (max over mean) of the radiated power is greater than two [Sugihara2007, Lehnen2015]. Because of these challenging requirements, research is underway in present tokamaks toward optimizing the radiated power fraction and radiation spatial uniformity during mitigation of VDEs and other types of disruptions [Hollmann2015]. One concern for ITER is that the present disruption mitigation system (DMS) port allocation of three upper ports and one midplane port will

not have sufficient spatial coverage for best radiation uniformity and radiated power fraction. This issue could be exasperated during downward VDEs, which will strike far from the ITER upper MGI ports. This has motivated the present study of VDE mitigation using MGI from ports at different poloidal locations.

Some previous work on MGI mitigation of VDEs has been performed. Clear signs of reduced vessel forces and reduced conducted heat loads were seen with MGI mitigation, compared with unmitigated VDEs. Reduced conducted heat loads were dominantly inferred indirectly from an increase in radiated power levels measured with fast bolometers. Within the scatter of the data, it appeared that roughly $> 90\%$ radiated power fraction was achieved. IR imaging of conducted heat loads on the wall was performed in a line scan across the lower divertor at one toroidal angle, but gave somewhat inconclusive results, partially due to the limited spatial coverage and partially due to plasma IR emission [Hollmann2013]. Additionally, preliminary experiments were performed on the relative effect of VDE mitigation using a MGI valve located above or below the plasma, with no clear difference seen between the two cases [Commaux2014].

Here, new experiments are presented which improve on the previous preliminary results of VDE mitigation using a MGI gas valve located above or below the plasma. These experiments improve on the previous work in three ways: (a) denser scans of the timing delay Δt_{MGI} between the MGI impact and VDE thermal quench (TQ); (b) data on all four permutations of valve location vs VDE direction (upward VDE with upper valve, downward VDE with lower valve, etc); and (c) improved IR camera data now with full poloidal spatial coverage. Overall, the data supports the previous preliminary finding that global mitigation of VDE conducted heat loads is not greatly improved by having a MGI valve located closer to the VDE impact point. As seen previously, MGI timing delay is found to be quite important, with earlier MGI giving improved mitigation. However, some degree of mitigation is observed even for relatively late MGI with impact during the TQ. The improved IR coverage shows that VDE conducted heat loads are dominantly on the plasma-limiting surfaces in the upper and lower divertors, as expected. Significantly larger apparent conducted heat loads are seen in upward VDEs compared with downward VDE; the origins of this are unclear at the moment, but could be due to differences in wall surface properties in the lower divertor versus the upper divertor. The improved IR data also demonstrates clearly the presence of plasma IR emission, which can confuse interpretation of IR images.

2. Experimental setup

The experiments presented here were performed in the DIII-D tokamak [Luxon2002]. The target plasmas were an “ITER-like” shape with low triangularity and lower single null. Deuterium plasmas heated with one neutral beam giving $P_{inj} = 1.7$ MW of heating power were used. Initial plasma current was $I_p = 1.3$ MA, initial thermal energy was $W_{th} = 0.6$ MJ, and initial magnetic energy was $W_{mag,int} = 0.7$ MJ inside the vacuum vessel and $W_{mag,ext} = 1.8$ MJ outside the vacuum vessel. At $t = 2000$ ms, the initially stable

plasma was given a downward (or upward) kick with the shaping coils. The elongated plasma then goes vertically unstable, drifting into the lower (or upper) divertor. In the absence of mitigation, these plasmas go into a disruption thermal quench (TQ) around time $t = 2025$ ms. Mitigation is performed here with massive gas injection (MGI) of neon gas. MGI is done from two different locations: an “R+1” port located above the plasma at toroidal angle $\phi = 15^\circ$ and an “R-2” port located below the plasma at toroidal angle $\phi = 135^\circ$. The drift duct geometry of the two systems was similar, but not identical, so the neon particle flux as a function of time is not exactly identical in the two cases. However, the pulse lengths (around 1.5 ms) of neon delivery were tuned to give similar total integrated neon fluence 250 - 300 Torr-L in each shot.

Figure 1 gives (a) an overview of principal diagnostics used here and (b) – (e) cartoons of the different mitigation combinations studied here (downward VDE mitigated by R+1 MGI, upward VDE mitigated by R+1 MGI, upward VDE mitigated by R-2 MGI, and downward VDE mitigated by R-2 MGI). The core thermal collapse timing is dominantly diagnosed with soft x-ray arrays. Radiated power is measured with AXUV photodiode arrays and foil bolometer arrays. Wall heat loads are measured with a mid-IR (3-5 μm) camera.

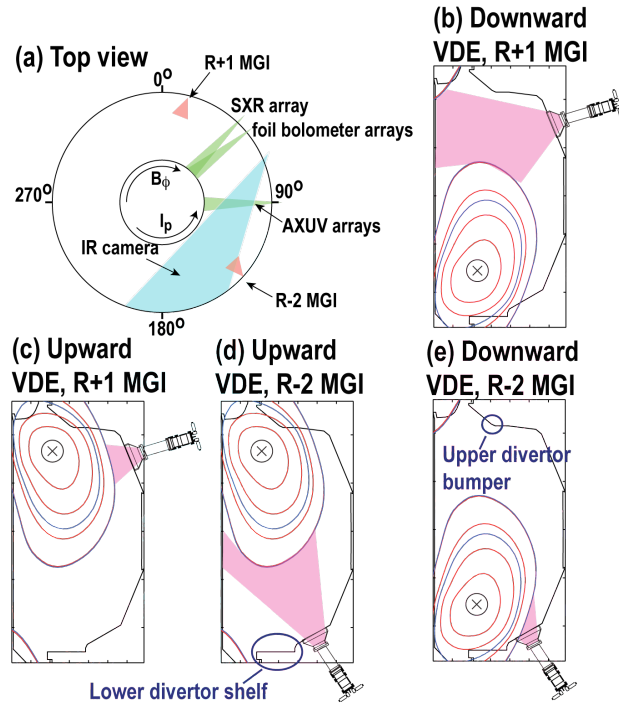


Fig. 1. (a) Overview of principal diagnostics and (b)-(e) schematics of different VDE direction/MGI location combinations.

An overview of time traces from a typical unmitigated VDE is shown in Fig. 2. A downward VDE is shown here, but the overall sequence is analogous for upward VDEs. The x-point disappears at $t \sim 2025$ ms and the plasma limits on the lower divertor shelf

(in the case of upper VDEs the plasma limits on the upper divertor bumper, see Fig. 1). At this time, the plasma TQ begins and the core temperature collapses, Fig 2(h). A radiation flash is seen, Fig. 2(g), and a spike in edge magnetics is seen, Fig. 2(i). The edge magnetics structure is dominantly low order ($n = 1$) toroidally, and maintains a fairly constant phase during the TQ, Fig. 2(j).

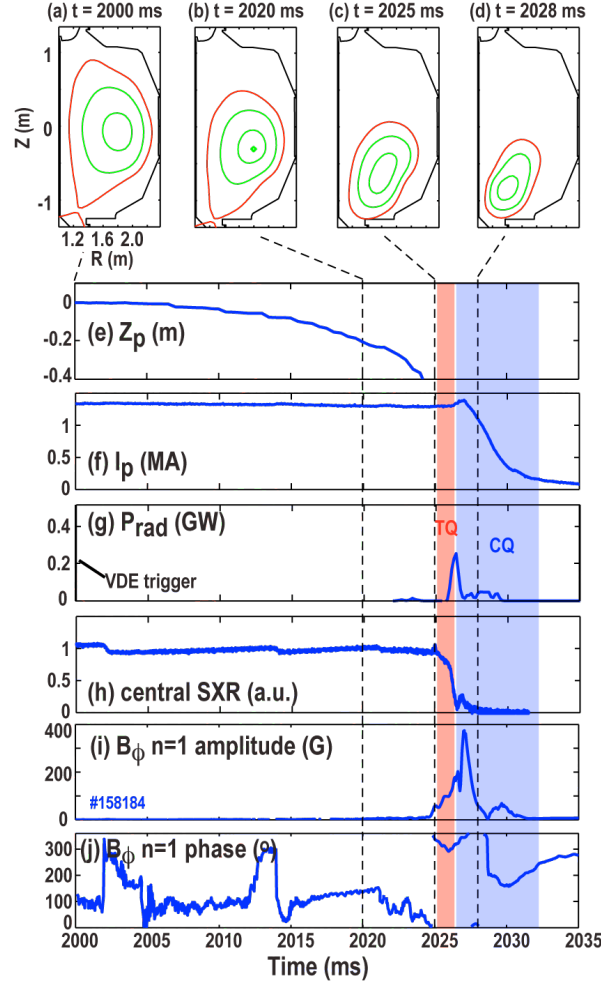


Fig. 2. Overview of unmitigated VDE experiment time traces showing (a)-(d) JFIT reconstructions of magnetic flux surfaces, (e) vertical position, (f) plasma current, (g) radiated power, (h) central SXR, (i) wall magnetics $n=1$ amplitude and (j) wall magnetics $n=1$ phase.

For comparison, time traces from a mitigated VDE are shown in Fig. 3. In this case, neon MGI is fired into the plasma before the VDE has caused the plasma to limit on the divertor and begin the TQ. The MGI “first light” impact of neon on the plasma edge occurs at $t = 2017.2$ ms. A rise in radiated power is observed, Fig. 3(g), and 1 ms later the plasma begins the TQ with the core temperature collapsing, Fig. 3(h). A spike in edge magnetic signals is also observed, Fig. 3(i), but the phase is not constant during the TQ, with clear rotation seen in Fig. 3(j) during the TQ. During the start of the CQ, the plasma elongates and maintains an x-point, Fig. 3(d), but typically limits on the divertor by the

middle of the CQ. The mitigation “timeliness” is characterized here by Δt_{MGI} , the delay between the MGI impact on the plasma edge and the expected TQ onset time if MGI had not been pre-emptively deployed; and example of Δt_{MGI} is shown in Fig. 3(e).

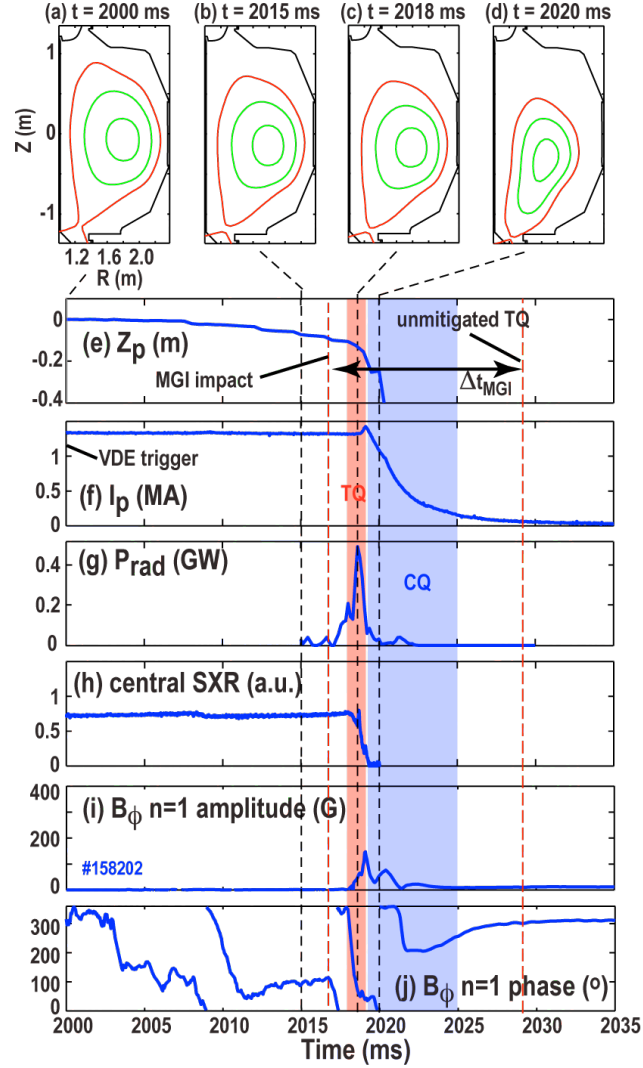


Fig. 3. Overview of mitigated VDE experiment time traces showing (a)-(d) JFIT reconstructions of magnetic flux surfaces, (e) vertical position, (f) plasma current, (g) radiated power, (h) central SXR, (i) wall magnetic $n=1$ amplitude and (j) wall magnetic $n=1$ phase.

3. Analysis of disruption IR camera data

The principal diagnostic used here to analyze conducted heat loads to the plasma wall is the DIII-D tangential IR camera [Lasnier2014]. The camera is kept to its full field of view during these experiments, thus covering much of the plasma cross section, but

limiting the acquisition rate to 8 ms per frame. Because this acquisition rate is slower than the TQ duration (~ 2 ms), the temperature decay of the post-disruption images is used to estimate the time-averaged TQ heat flux to the walls. In the analysis, the temperature decay at each pixel is fit as a function of time after the disruption is over, assuming a separable contribution from the initial temperature of the surface (due to steady-state plasma heating) plus the contribution from the disruption heat pulse:

$$T(t) = T_{\infty} + (T_0 - T_{\infty})\exp(-(t - t_0)/\tau_{\infty}) + \frac{\Delta t \Delta q}{\sqrt{\pi \rho c_p \kappa (t - t_0)}} \quad , \quad (1)$$

where T_{∞} is the final wall temperature (taken to be 20° C), T_0 is the initial wall temperature (calculated from the data), Δt is the length of the disruption heat pulse (taken to be 2 ms), and Δq is the disruption heat flux (the free parameter in the fit). Here we have ignored blackbody radiation, lateral heat diffusion, and variation of wall properties ρ , c_p , and κ with temperature (typical values for amorphous graphite at 200 C are assumed). t_0 is the time of the disruption heat pulse and is taken to be at the I_p spike. The exponential term in Eq. (1) is the approximate form expected for the cooling of a semi-infinite slab heated on one surface with the heat source suddenly switched off; while the $1/\sqrt{t}$ term is the form expected for the cooling of a semi-infinite slab suddenly heated on the surface by a delta function heat pulse [Carslaw1995]. The background temperature cooling time constant τ_{∞} is fit experimentally from lower divertor pixels with upward VDEs, giving points with a high initial temperature but then little additional TQ heating. Typically, $\tau_{\infty} \approx 170$ ms is found, as shown in Fig. 4(a). A sample fit where both initial wall temperature and disruption heat pulse are significant is shown in Fig. 4(b), where the black curve labeled “background” is the contribution of the exponential decay only and the red curve labeled “background + heat pulse” includes the $1/\sqrt{t}$ TQ heat pulse decay term in Eq. (1) also.

Volume IR emission from the plasma, both prior to the disruption and during the disruption, can affect this analysis. Pre-disruption IR emission will give an incorrect apparent value of T_0 , the initial wall temperature. To correct for this, spatial pixels where the apparent initial temperature T_0 results in a background temperature decay which lies above the data are corrected by lowering T_0 until a minimum value is reached which lies below all data points in the post-disruption temperature decay. An example of this is shown in Fig. 4(c), where the initial apparent wall temperature gives a background decay shown by the blue dashed curve lying well above the post-disruption data points. Lowering T_0 until the background curve lies below all the data points gives a more physically realistic background and total temperature decay fit.

To avoid volume IR emission during the disruption, the fits to Eq. (1) are performed only on data points past the end of the CQ. Frequently, the data point(s) falling during the CQ time window are observed to lie well above this fit; this is interpreted as being at least partially due to volume IR emission during the CQ. An example of this is shown in Fig.

4(d), where a very large deviation from the post-disruption decay fit is seen during the CQ.

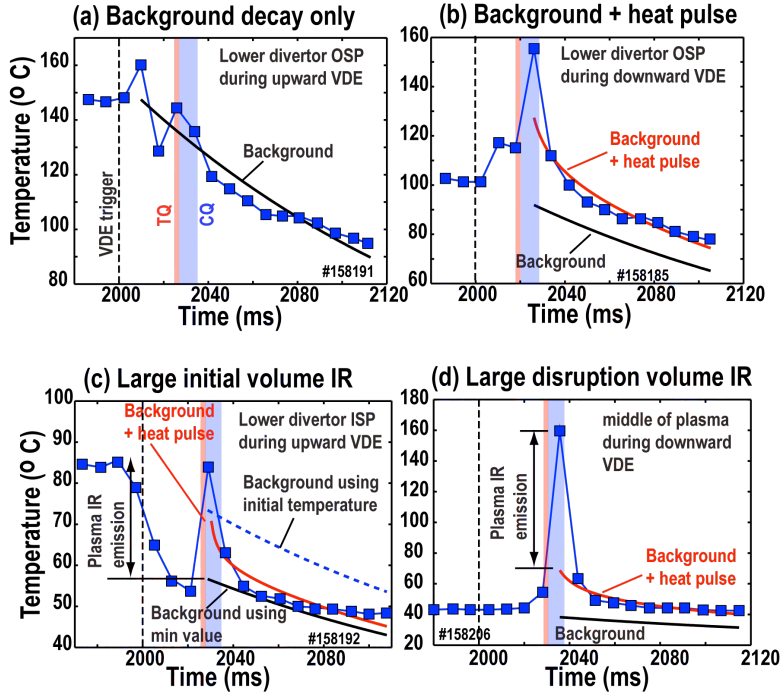


Fig. 4. Examples of fits to post-disruption IR data time sequences at different locations showing (a) background temperature decay in location with negligible disruption heating, (b) total temperature decay in location with comparable initial and disruption heat pulse heating, (c) temperature decay fits in location with significant initial plasma IR emission, and (d) temperature decay fits in location with significant disruption plasma IR emission.

Figure 5 shows an example of IR images and resulting reconstructed disruption heat flux for an unmitigated upward VDE. Figure 5(a) gives an example pre-disruption IR image, showing lower divertor hot spots. Figure 5(b) then shows an example during-disruption IR image, and Fig. 5(c) shows an image of the resulting calculated disruption heat flux. The black squares in each image are used to cover the optical blind spot of the IR camera periscope system and also the bright heated glow discharge heating element. Figure 5(d) shows a CAD model of the IR camera view, showing the slight distortion of the straight center post caused by the camera optics [Lasnier2014].

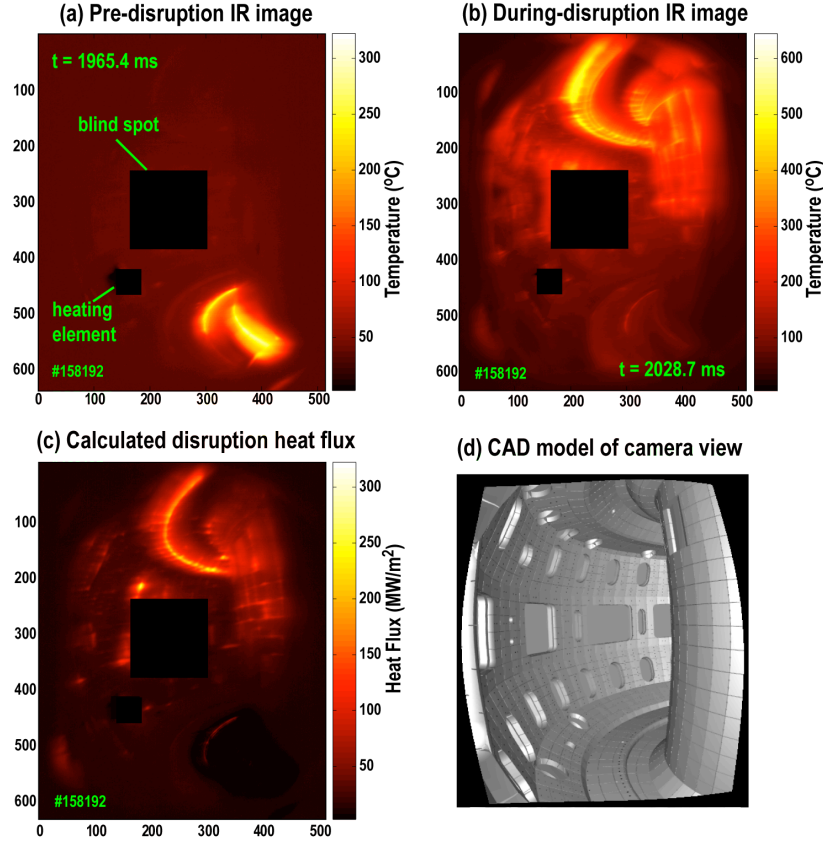


Fig. 5. Example IR images for an unmitigated upward VDE showing: (a) pre-disruption image, (b) during-disruption image, (c) calculated disruption heat flux, and (d) CAD model of IR camera view.

Figure 6 gives examples of (a) pre-disruption plasma IR emission and (b) during-disruption plasma IR emission obtained from the time-decay analysis discussed earlier. It can be seen that pre-disruption plasma IR emission tends to be dominant in the inner strike point. Typically, the inner strike point detaches very easily in DIII-D, leading to very cold dense plasma there which could be expected to contain cold hydrocarbon molecules with strong IR emission lines. The disruption plasma IR emission is typically found more distributed throughout the vacuum vessel volume, as can be seen in Fig. 6(b). The origins of this emission are not known, but it appears to be strongest in mitigated disruptions so is perhaps a result of IR line emission by neutral neon, e.g. Ne-I (4035 nm).

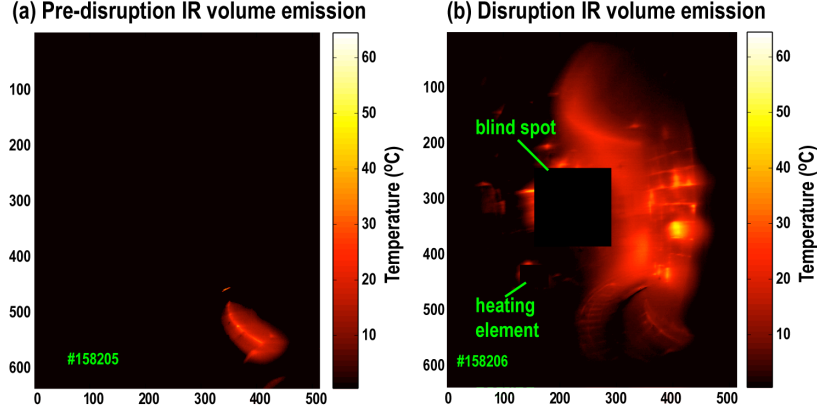


Fig. 6. Images of (a) pre-disruption plasma IR emission and (b) during-disruption plasma IR emission.

The spatial distribution of conducted heat loads in disruptions is very important. For example, if there is a fixed toroidal phase at which the conducted heat loads peak, this could result in greatly reduced wall lifetime at that location. Figure 7 shows examples of disruption heat loads for partially mitigated ($\Delta t_{MGI} \approx -2$ ms) upward and downward VDEs. As expected, the downward VDE heat loads are dominantly on the lower divertor shelf (outlined by green lines in Fig. 7(a), showing toroidal angles $\phi = 105^\circ - 180^\circ$), while the upward VDE heat loads are dominantly on the upper divertor bumper (outlined by green lines in Fig. 7(d), showing toroidal angles $\phi = 100^\circ - 190^\circ$). The heat loads in these outlined regions are presumably dominantly conducted; radiated heat loads are expected to have a broader radial structure. Toroidal and radially averaged heat loads are shown in Fig. 7(b,c,e,f) to highlight the radial and toroidal structure of the conducted heat loads. It can be seen that the radial structure of the downward VDE has a double hump structure, possibly due to non-axisymmetries in the structure of the plasma during the TQ; this double hump is not observed in the upward VDE. Toroidally, some degree of variation is seen in the heat loads. Attempts were made to obtain a $n=1$ heat load phase with sine fits, as shown in Fig. 7(c) and 7(f), although the relatively limited toroidal coverage of the data makes these fits somewhat poorly constrained.

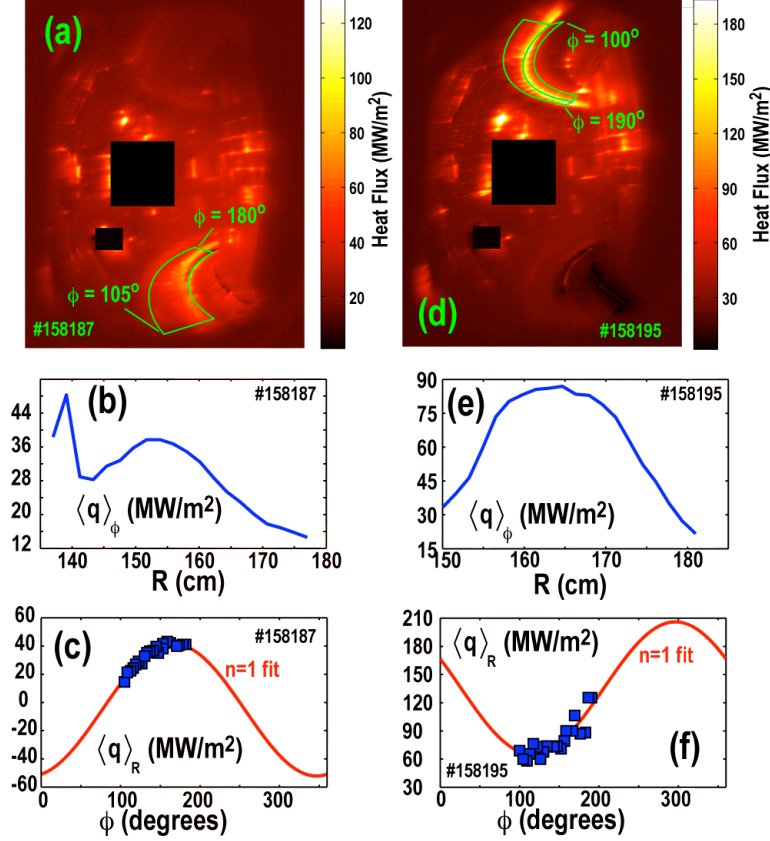


Fig. 7. Comparisons of downward and upward VDE conducted heat load distributions showing: (a) disruption heat flux, (b) radial distribution of heat flux, and (c) toroidal distribution of heat flux with $n=1$ fit. (d)-(f) are equivalents for upward VDE. Green boxes in (a) and (d) are regions over which toroidal and radial averages are calculated.

4. Discussion

Figure 8 gives an overview of 0D trends in effectiveness of MGI mitigation of VDEs. The data are plotted as a function of the MGI impact delay Δt_{MGI} . Figure 8(a) shows the TQ radiated energy estimated by tomography of the fast bolometers. Figure 8(b) shows the total radiated energy estimated by tomography of the slow bolometers. The slow bolometer data serves as an independent cross check confirming that radiated energy loss is decreasing with reduced MGI delay time. Figure 8(c) gives the peak amplitude of the vacuum vessel vertical motion during the disruption, giving a qualitative picture of vessel forces. Figure 8(d) shows the peak conducted heat flux. To average over small local hot spots, an approximate “peak” heat flux is defined: $\text{peak } q_{cond} \equiv \int q^2 R dR d\phi / \int q R dR d\phi$, where the spatial integral is over the divertor areas shown by green lines in Fig. 7(a) or 7(d). Figure 8(e) shows the total conducted heat flux. This is estimated by integrating the heat flux over the divertor and then assuming toroidal symmetry to include the remainder of the vessel. An attempt to subtract the radiated heat load contribution in a crude way is made by subtracting off the minimum heat flux to the divertor from the data (assuming a

constant radiative heating over the divertor surface area). Finally, Fig. 8(f) gives the magnitude of the plasma current decay rate. This is taken 1 ms after the I_p spike with a 1 ms smoothing window. The current decay rate gives a rough picture of the amount of impurities in the CQ plasma, with larger impurity levels giving a lower temperature and a faster current decay rate. In Fig. 8, for plotting purposes, the data with $\Delta t_{MGI} = 5$ ms actually corresponds to unmitigated VDE disruptions with no MGI.

Overall, Fig. 8 indicates that there is no significant global improvement in mitigation effectiveness of VDEs when using a MGI port closer to the VDE direction. For example, the peak TQ heat flux, Fig. 8(d), shows no clear difference when mitigating upward VDEs with upper (R+1) or lower (R-2) MGI; other global indicators similarly show no systematic difference when comparing upper vs lower MGI. In contrast, MGI timing delay Δt_{MGI} clearly has a large effect, with earlier MGI resulting in higher radiated energies, lower conducted heat fluxes, and lower vessel motion. Even injecting during the TQ ($\Delta t_{MGI} = 0$) appears to have some small mitigation benefit over not using MGI at all. This data thus suggests that TQ mixing of heat and impurities is very effective even during “hot” VDEs where the TQ occurs when the plasma is limited on the divertor. This effective TQ mixing tends to smooth out the effect of injection location on global disruption mitigation indicators, although there may well still be differences in the poloidal radiation structure; these more subtle differences are not pursued in the present analysis.

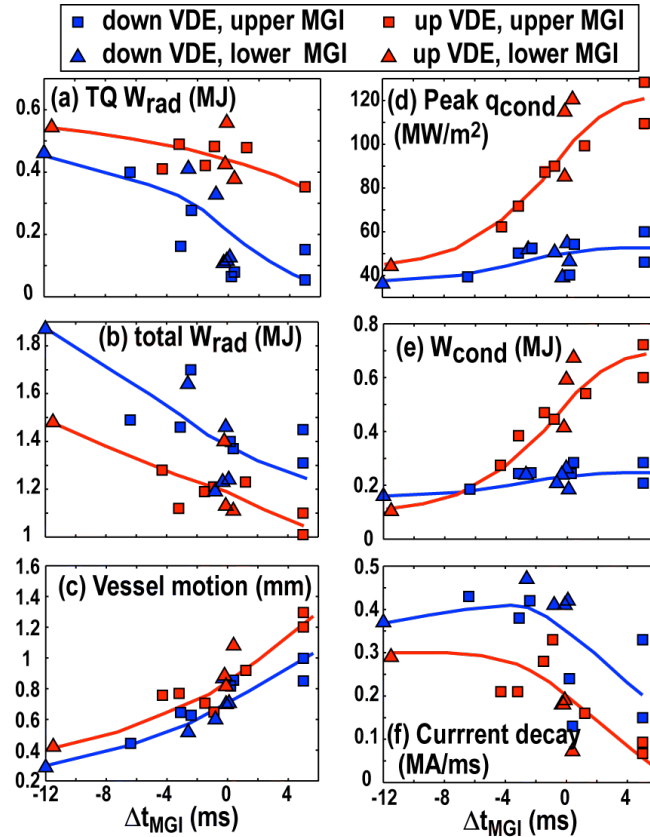


Fig. 8. Global trends in VDE mitigation effectiveness for different VDE direction/MGI location combinations as a function of MGI trigger delay Δt_{MGI} showing (a) TQ radiated energy, (b) total radiated energy, (c) vessel vertical motion, (d) peak conducted heat flux, (e) total conducted energy, and (f) CQ current decay rate.

One trend in the data which is not understood at present is the large difference in apparent conducted heat loads seen between upward and downward VDEs, Fig. 8(e). In the case of upward VDEs, the data appears to be roughly consistent between different diagnostics: total radiated energy goes down by perhaps 0.5 MJ moving from early to late mitigation, Fig. 8(b); at the same time conducted energy increases by perhaps 0.5 MJ, Fig. 8(e). However, in the case of downward VDEs, the total radiated energy also decreases by 0.5 MJ but the conducted energy appears to increase by only about 0.1 MJ. It is possible that there is some difference in induced energy loss between the two cases: it can be seen that there is a slight increase in current decay rate for downward VDEs, Fig. 8(f), and this might be expected to result in greater loss of external magnetic energy into conducting structures (vessel wall, shaping coils, etc). This seems an unlikely explanation though, since most of the conducted heat loss is expected to come during the TQ from the initial 0.6 MJ of available thermal energy, not from magnetic energy during the CQ.

Another possibility is that there is a large difference in toroidal phase of conducted heat loads between the two cases, i.e. that much of the conducted heat load for downward VDEs is consistently out of the field of view of the IR camera. To investigate this, the TQ toroidal phase of the plasma current as well as the conducted heat loads were plotted in Fig. 9(a) and 9(b). In both cases, $n = 1$ fits are used. For the current channel phase, poloidal B is used from internal coils and from the toroidal array of probes closest poloidally to the impact point of the VDE. It can be seen that there is a clear trend in preferred phase of the plasma current channel. It does appear that this preferred phase appears to fall more within the view of the IR camera ($\phi = 100^\circ - 190^\circ$) for upward VDEs and not for downward VDEs, Fig. 9(a). However, fits to the conducted heat phase (such as shown in Fig. 7) do not appear to show a behavior consistent with the current channel phase. This may be due to the reduced toroidal coverage of the IR camera giving poor fits, or due to a real effect. Previous analysis did show a correlation between the toroidal phase of radiated power and the plasma current channel in MGI shutdowns [Shiraki2015]; however, a correlation between toroidal phase of plasma current and conducted heat loads has not been demonstrated yet here or elsewhere. Previous analysis based on shot-shot variation of VDE conducted heat loads at a single (line-scan) toroidal location suggested that toroidal variation of conducted heat loads was fairly small $\sim 10\%$ [Hollmann2013]; this appears inconsistent with the large amplitude $n = 1$ fits of Fig. 7 and large shot-shot variation in phase of Fig. 9(b).

Another possibility is that the upper and lower divertor surfaces have quite different IR emissivities. Here, we assume that all graphite surfaces have the same (constant) properties for emissivity, thermal conductivity, etc. However, the lower divertor, being subjected to larger heat and particle fluxes, could well have different material properties than the upper divertor; attempts to investigate this possibility will be made in future

experiments.

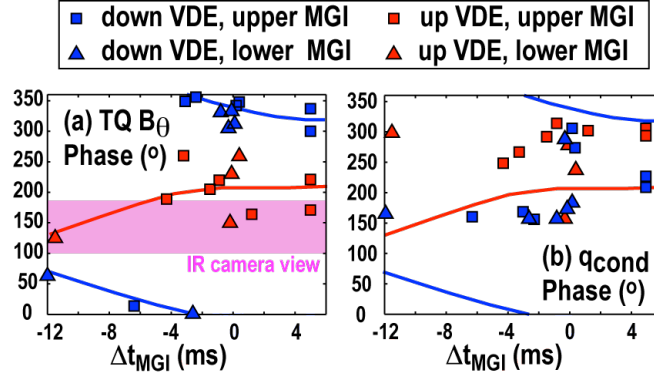


Fig. 9. Trends in mid-TQ toroidal phase as a function of MGI trigger delay Δt_{MGI} showing (a) poloidal magnetic field phase and (b) conducted heat load phase. Curves in (b) are same as fit to data in (a) for comparison.

5. Summary

Intentionally triggered upward- and downward-moving vertical displacement events (VDEs) leading to disruptions were pre-emptively mitigated with neon massive gas injection (MGI) coming from either above or below the plasma. Improved coverage of resulting conducted heat loads was obtained with new full-chamber IR imaging. Global indicators of disruption mitigation effectiveness (conducted heat loads, radiated energy, and vessel motion) do not show a clear improvement when mitigating with gas jets closer to the VDE impact region. This is good news for ITER in that it suggests that the present ITER DMS port allocation of three upper ports and one midplane port will be as effective as a possible lower port for mitigating downward VDE heat loads. The data clearly demonstrate the need for sufficiently early MGI triggering for effective VDE heat load mitigation; however, with an expected VDE timescales of 100 ms or more, timely MGI or SPI mitigation of VDEs should be easy to achieve in ITER.

Acknowledgements

Helpful suggestions from M. Lehnen are acknowledged. This work was supported in part by the US Department of Energy under DE-FG02-07ER54917, DE-FC02-04ER54698, DE-AC05-00OR22725, [DE-AC52-07NA27344](#) and DE-AC05-06OR23100.

References

- [Hender2007] T. C. Hender, J. C. Wesley, J. Bialek, A. Bondeson, A.H. Boozer, R.J. Buttery, A. Garofalo, T.P. Goodman, R.S. Granetz, Y. Gribov, O. Gruber, M. Gryaznevich, G. Giruzzi, S. Guenter, N. Hayashi, P. Helander, C.C. Hegna, D.F. Howell, D.A. Humphreys, G.T.A. Huysmans, A.W. Hyatt, A. Isayama, S.C. Jardin, Y. Kawano, A. Kellman, C. Kessel, H.R. Koslowski, R.J. La Haye, E. Lazzaro, Y.Q. Liu, V. Lukash, J. Manickam, S. Medvedev, V. Mertens, S.V. Mirnov, Y. Nakamura, G. Navratil, M. Okabayashi, T. Ozeki, R. Paccagnella, G. Pautasso, F. Porcelli, V.D. Pustovitov, V. Riccardo, M. Sato, O. SAuter, M.J. Schaffer, M. Shimada, P. Sonato, E.J. Strait, M. Sugihara, M. Takechi, A.D. Turnbull, E. Westerhof, D.G. Whyte, R. Yoshino, H. Zohm, and the ITPA MHD disruption and magnetic control topical group, *Nucl. Fusion* **47**, S128 (2007).
- [Hollmann2011] E. M. Hollmann, G. Arnoux, N. Commaux, N.W. Eidietis, T. Evans, R.S. Granetz, A. Huber, D.A. Humphreys, V.A. Izzo, A.N. James, T.C. Jernigan, M. Lehnen, G. Maddaluno, R. Paccagnella, P.B. Parks, V. Phillips, M.L. Reinke, D.L. Rudakov, F. Saint-Laurent, V. Sizyuk, E.J. Strait, J.C. Wesley, C.P.C. Wong, and J.H. Yu, *J. Nucl. Mater.* **415**, S27 (2011).
- [Taylor1999] P.L. Taylor, A.G. Kellman, T.E. Evans, D.S. Gray, D.A. Humphreys, A.W. Hyatt, T.C. Jernigan, R.L. Lee, J.A. Leuer, S.C. Luckhardt, P.B. Parks, M.J. Schaffer, D.G. Whyte, and J. Zhang, *Phys. Plasmas* **6**, 1872 (1999).
- [Commaux2010] N. Commaux, L.R. Baylor, T.C. Jernigan, E.M. Hollmann, P.B. Parks, D.A. Humphreys, J.C. Wesley, and J.H. Yu, *Nucl. Fusion* **51**, 063007 (2011).
- [Sugihara2007] M. Sugihara, M. Shimada, H. Fujieda, Yu. Gribov, K. Ioki, Y. Kawano, R. Khayrutdinov, V. Lukash, and J. Ohmori, *Nucl. Fusion* **47**, 337 (2007).
- [Lehnen2015] M. Lehnen, K. Aleynikov, P.B. Aleynikov, D.J. Campbell, P. Drewelow, N.W. Eidietis, Yu. Gasparyan, R.S. Granetz, Y. Gribov, N. Hartmann, E.M. Hollmann, V.A. Izzo, S. Jachmich, S.H. Kim, M. Kocan, H.R. Koslowski, D. Kovalenko, U. Kruezi, A. Loarte, S. Maruyama, G.F. Matthews, P.B. Parks, G. Pautasso, R.A. Pitts, C. Reux, V. Riccardo, R. Roccella, J.A. Snipes, A.J. Thornton, P.C. de Vries, and EFDA JET contributors, “Disruptions in ITER and strategies for their control and mitigation,” accepted by *J. Nucl. Mater.* (2014).
- [Hollmann2015] E.M. Hollmann, P.B. Aleynikov, T. Fülöp, D.A. Humphreys, V.A. Izzo, M. Lehnen, V.E. Lukash, G. Papp, G. Pautasso, F. Saint-Laurent, and J.A. Snipes, *Phys. Plasmas* **22**, 021802 (2015).
- [Hollmann2013] E.M. Hollmann, N. Commaux, N.W. Eidietis, D.A. Humphreys, T.J. Jernigan, C.J. Lasnier, R.A. Moyer, R.A. Pitts, M. Sugihara, E.J. Strait, J. Watkins, and J.C. Wesley, *Phys. Plasmas* **20**, 062501 (2013).
- [Commaux2014] N. Commaux, L.R. Baylor, T.C. Jernigan, E.M. Hollmann, D.A. Humphreys, J.C. Wesley, V.A. Izzo, N.W. Eidietis, C.J. Lasnier, R.A. Moyer, P.B. Parks, C.R. Foust, S. Combs, S.J. Meitner, *Phys. Plasmas* **21**, 102510 (2014).
- [Luxon2002] J. L. Luxon, *Nucl. Fusion* **42**, 614 (2002).
- [Lasnier2014] C.J. Lasnier, S.L. Allen, R.E. Ellis, M.E. Fenstermacher, A.G. McLean, W.H. Meyer, K. Morris, L.G. Seppala, K. Crabtree, and M.A. van Zeeland, *Rev. Sci. Instrum.* **85**, 11D855 (2014).

[Carslaw1995] H.S. Carslow and J.C. Jaeger, Conduction of Heat in Solids, 2nd Ed. (Oxford, Claredon, 1995).

[Shiraki2015] D. Shiraki, N. Commaux, L.R. Baylor, N.W. Eidietis, E.M. Hollmann, V.A. Izzo, R.A. Moyer, and C. Paz-Soldan, “Characterization of MHD activity and its influence on radiation asymmetries during massive gas injection in DIII-D,” submitted to Nucl. Fusion (2014).